

JGR Atmospheres

RESEARCH ARTICLE

10.1029/2020JD034016

Key Points:

- The timing of secondary eyewall formation is sensitive to the magnitude of shortwave radiation
- Shortwave radiation can modify secondary eyewall formations by reducing the extent and magnitude of diabatic heating in convective rainbands
- The interactions between shortwave radiation and cloud microphysics are critical for simulating eyewall replacement cycles

Correspondence to:

B. C. Trabing,
btrabing@colostate.edu

Citation:

Trabing, B. C., & Bell, M. M. (2021). The sensitivity of eyewall replacement cycles to shortwave radiation. *Journal of Geophysical Research: Atmospheres*, 126, e2020JD034016. <https://doi.org/10.1029/2020JD034016>

Received 3 OCT 2020

Accepted 19 MAR 2021

Author Contributions:

Conceptualization: B. C. Trabing, M. M. Bell
Formal analysis: B. C. Trabing
Funding acquisition: M. M. Bell
Investigation: B. C. Trabing
Methodology: B. C. Trabing
Project Administration: M. M. Bell
Resources: M. M. Bell
Supervision: M. M. Bell
Validation: B. C. Trabing
Visualization: B. C. Trabing
Writing - original draft: B. C. Trabing
Writing - review & editing: M. M. Bell

The Sensitivity of Eyewall Replacement Cycles to Shortwave Radiation

B. C. Trabing¹  and M. M. Bell¹ 

¹Department of Atmospheric Sciences, Colorado State University, Fort Collins, CO, USA

Abstract The sensitivity of tropical cyclone secondary eyewall formation (SEF) and subsequent eyewall replacement cycles (ERCs) to shortwave radiation is examined in this study by varying the solar constant and diurnal cycle at different times prior to an ERC using idealized simulations from the Weather Research and Forecasting model. The magnitude of shortwave radiation plays an important role in modifying the timing of the SEF with nonlinear interactions amplifying the SEF formation differences at longer lead-times. Shortwave radiation has a delaying effect on the SEF and ERC primarily through its modifications of the distribution of convective and stratiform heating profiles in the rainbands. Shortwave radiation reduces both the area and diabatic heating of convection in the model domain, while increasing the amount of stratiform precipitation that has weaker low-level cooling and upper-level heating rates. The primary mechanism by which shortwave radiation reduces the diabatic heating profile and frequency of convection in the rainbands is through heating of the mid-upper troposphere which stabilizes the region and reduces convective available potential energy.

1. Introduction

It is now understood that eyewall replacement cycles (ERCs) are a common phenomenon in mature tropical cyclones (TCs). A secondary eyewall formation (SEF) always precedes eyewall replacement cycles and is considered the starting point of the ERC. The strength of tangential winds near the primary eyewall typically decay while tangential winds near the secondary eyewall intensify during an ERC. Once the secondary eyewall eclipses the intensity of the primary eyewall there is a rapid outward expansion of the radius of maximum winds (RMW) and often a reintensification of the maximum surface winds. During an ERC the weakening of the primary eyewall reduces the maximum intensity of the TC, while the strengthening secondary eyewall expands the wind field and increases the overall integrated kinetic energy of the system (Sitkowski et al., 2011). Changes in the wind field caused by ERCs are critical to forecast because a broader wind field means that damage could extend over a larger area. The prediction of ERCs remain a challenge for operational forecasters because they are driven by vortex-scale processes that are internally regulated and often short lived (Kossin & DeMaria, 2016). Kossin and DeMaria (2016) showed that ERCs introduce substantial intensity forecast errors in the Statistical Hurricane Intensity Prediction Scheme (SHIPS), which is one of the primary intensity guidance models used by the National Oceanic and Atmospheric Administration/National Hurricane Center (NOAA/NHC) (DeMaria et al., 2005). Kossin and DeMaria (2016) subsequently developed a new version of SHIPS (E-SHIPS) that incorporates the Microwave-based Probability of Eyewall Replacement Cycle (M-PERC; Herndon et al., 2020) model to predict the weakening associated with ERCs. Accurately forecasting the onset time of ERCs is essential to the application of E-SHIPS to reduce intensity forecasts errors. In order to improve intensity forecasts, numerical weather prediction models need to accurately capture the onset and duration of ERCs.

The resolution and physics of numerical weather prediction models are continually improving and many hurricane forecast models are now able to explicitly simulate ERCs. It is unclear how sensitive ERCs may be to individual radiation or microphysics schemes. Recent work by Tang et al. (2017) showed that the SEF in Hurricane Edouard (2014) did not occur when shortwave radiation was removed from the simulation. It was shown that shortwave radiation acts to stabilize the mid-upper troposphere, suppressing convective development in the moat region over the 48 h prior to the SEF. The sensitivity of SEF and subsequent ERC to diurnal shortwave radiation in an idealized framework has not yet been addressed in the literature, which is the goal of the present study. The current study aims to evaluate the sensitivity of SEFs to radiation in an idealized framework in order to diagnose the impacts of diurnal radiation on ERC timing, and TC intensity.

It is well known that shortwave radiation plays an important role in the diurnal cycle of convective clouds, but how this role impacts the structure, intensity, or genesis of TCs is often case dependent. During tropical cyclogenesis, radiation can influence individual cloud clusters and convective cells because a cirrus canopy has not yet developed. Without the upper-level cloud canopy the environment can efficiently cool due to longwave radiation, which has been shown to increase the relative humidity (RH) and increase rates of subsequent tropical cyclogenesis (Sundqvist, 1970; Craig, 1996; Melhauser & Zhang, 2014; Tang & Zhang, 2016; Bell & Montgomery, 2019). Other studies have suggested the differential radiative heating between cloudy and cloud-free regions could promote stronger low-level convergence into the cloudy region to generate deep convection (Gray & Jacobson, 1977; Nicholls, 2015). Bu et al. (2014) found that weak but continuous longwave warming in the cirrus canopy was responsible for strengthening the TC outflow and inducing a vertical circulation throughout the outer core that favored the development of deep convection. Fovell et al. (2016) reaffirmed the results of Bu et al. (2014) using several idealized models, showing that the longwave warming within the cirrus canopy was important for expanding the tangential wind field of TCs by promoting outer core convection and increasing RH through weak tropospheric ascent. Direct shortwave heating in the mid-upper tropospheric clouds in contrast acts to stabilize the layer and reduce convective precipitation (Xu & Randall, 1995). Shortwave heating within the cirrus canopy near the vortex center can also generate anomalous circulations that enhance or reduce the TC secondary circulations and generate propagating inertial buoyancy waves (Dunion et al., 2014; Navarro et al., 2017; Ruppert & O'Neill, 2019). Radiation is important to consider on ERCs because of the multiple ways by which it can modify TC intensity and structure.

Several mechanisms have been proposed on what causes SEFs, although a clear consensus on the primary mechanism has not yet been reached. Proposed mechanisms on SEF generation have been focused on the importance of the stagnation radius of the vortex Rossby wave energy dispersion, the dynamical response of a balanced vortex to latent heating outside the eyewall, and the unbalanced dynamics within the boundary layer (H. Wang et al., 2016, and references therein). The unbalanced dynamics of the boundary layer in initiating and sustaining secondary eyewall convection shown in Huang et al. (2012) occurred following the broadening of the wind field caused by convective heating above the boundary layer. Regardless of the mechanism, axisymmetrization of rainband convection is required for SEF, although recent studies have suggested that stratiform clouds may also be important for initiating SEF (Didlake et al., 2018; Didlake & Kumjian, 2018). Zhu and Zhu (2014) showed that outer rainband diabatic heating from convection induces large positive tangential wind tendencies leading to the formation of secondary wind maxima. Zhu and Zhu (2014) further used the Eliassen model (Eliassen, 1952) to demonstrate that outer rainband convection must reach a certain strength relative to the eyewall convection before it can initiate and drive a secondary wind maximum to complete an ERC. Once the deep convection in the secondary eyewall is of sufficient strength and nearly axisymmetric, the inflow of warm moist air into the primary eyewall is reduced causing the primary eyewall to weaken and be replaced by the secondary eyewall (Houze et al., 2007).

Although Tang et al. (2017) found that the suppression of convection in the moat region is the most important effect of shortwave radiation on SEF occurrence, we propose that there is another mechanism controlling the timing of SEF and therefore the onset of ERCs. It is hypothesized that on short time scales the direct shortwave radiative heating in the expansive upper-level cloudy region stabilizes the upper-troposphere and reduces convective available potential energy (CAPE), which diminishes the strength of outer core convection. Shortwave heating in the outer core produces a less favorable environment for convection, yielding less total condensational heating in the rainbands, a slower expansion of tangential winds, and ultimately a delayed secondary eyewall formation and eyewall replacement cycle. The shortwave radiative effect on SEFs is suggested to be through a modification of the rainband diabatic heating profile.

The paper is organized as follows. In the following section, the setup of the idealized model and experimental design will be detailed with additional sensitivity tests. Section 3 will show the sensitivity of the ERCs to shortwave radiation while Section 4 will diagnose the factors controlling changes to TC structure and intensity. Section 5 focuses on the effects of shortwave radiation on the bulk properties of convective and stratiform clouds. Section 6 will summarize and discuss the conclusions from this work.

2. Experiments

To investigate the influences of radiation on SEFs and ERCs, idealized experiments are conducted using the Advanced Research version of the Weather Research and Forecasting (WRF-ARW; version 3.7.1; Skamarock et al., 2008) model. In the full-physics idealized simulations performed by Trabing et al. (2019), TCs developed a secondary eyewall without any added perturbations to the model. In Trabing et al. (2019), ensembles were performed with full radiation, longwave only radiation, and no radiation with three different tropopause temperatures each. From the ensemble members that underwent an ERC, the first ensemble member is selected from the experiment with a tropopause temperature of 199.6 K to be the “Control” for this study. It is noted that when full diurnal radiation was included the intensity variability due to small water vapor perturbations was small, so the following results are not sensitive to the specific selection of any individual ensemble member.

The experimental setup for the idealized WRF simulations can be found in Trabing et al. (2019) but will be briefly summarized here for completeness. The simulations were conducted with two-way nested, doubly-periodic domains with 18, 6, and 2 km resolution in the horizontal and 30 stretched vertical levels reaching 25 km in altitude. The outer domain of the simulations extends 5400 km in the horizontal and employs the New Tiedtke convective parameterization due to its relatively coarse resolution (Tiedtke, 1989). Idealizations are made such that the sea surface temperature (SST) is fixed at 301 K, there is no background flow, and the Coriolis parameter is fixed ($f = 5 \times 10^{-5} \text{ s}^{-1}$). The simulations are initialized with a weak vortex which is the same as that in Rotunno and Emanuel (1987) and subsequently integrated for eight days beginning at local noon on 3 July. The Thompson aerosol-aware microphysics (Thompson & Eidhammer, 2014) and the Yonsei University planetary boundary layer scheme (Hong et al., 2006) were employed.

The radiation schemes used in this experiment are the Rapid Radiative Transfer Model (RRTM) for longwave radiation (Mlawer et al., 1997) and the Dudhia shortwave radiation scheme (Dudhia, 1989). The RRTM and Dudhia radiation packages are the same schemes used in Tang et al. (2017). Both schemes use the plane-parallel assumption in calculating radiative fluxes while the solar zenith angle for shortwave flux calculation is horizontally homogeneous for each time step. To test the sensitivity of ERCs to shortwave radiation we restart the Control simulation at two different times prior to the ERC with modifications to the radiation packages. We restart the Control simulation at the 48 h mark when the TC is rapidly intensifying and at the 96 h mark when the TC is near its maximum intensity and would be considered a mature TC. Two different times are examined because the effects of radiation on TC intensity and ERCs may be subjective relative to the developmental stages of the TC and the formation of a cirrus canopy.

From the 48 and 96 h restarts, we first turn off only the shortwave radiation from the Dudhia scheme, which means that we have created a scenario where it is only night, and will be referred to as “NoSW48” and “NoSW”. To better understand how shortwave radiation influences the ERC, we next vary the amount of shortwave heating by changing the “solar constant” in the radiation driver of WRF. The initial solar constant from the control of 1370 W m^{-2} is halved (685 W m^{-2}), amplified by 50% (2055 W m^{-2}), and doubled (2740 W m^{-2}). These experiments will be referred to as “ $0.5 \times \text{SW}$ ”, “ $1.5 \times \text{SW}$ ”, and “ $2 \times \text{SW}$ ” by the ratio of modification to the solar constant, respectively. All of the experiments referenced herein are listed in Table 1. By changing the solar constant we can directly test the sensitivity of ERCs to the magnitude of shortwave heating but note that the factors changing the solar constant do not directly translate to the same exact factor of heating, which will be modified by cloud feedbacks. Figure 1a shows average shortwave heating rates for each experiment over a 24 h period highlighting the changes to the magnitude of radiative heating due to the changes in the solar constant. Overall the largest differences in the shortwave radiative heating rates are within the thick upper-level clouds and peaks at 14 km at the beginning of the restart experiments.

Additional sensitivity tests are conducted to estimate the effects of the diurnal cycle on the ERC and to the timing of the modification relative to the diurnal cycle. The first sensitivity test is to completely remove the diurnal cycle of shortwave radiation. We remove the diurnal cycle by fixing the solar zenith angle and reducing the solar constant such that the daily integrated solar insolation is the same as the control. By reducing the solar constant but allowing shortwave heating at all time steps, we are essentially reducing the average longwave cooling rates. The same methodology is used in Ruppert and O’Neill. (2019) for examining the circulation changes in simulated TCs due to the diurnal cycle. We use this method on each of

Table 1*Description of the Experiments and Abbreviated Names Referred to in This Study*

Name	Experiment
NoSW48	Restart at the 48 h mark with no solar radiation
0.5×SW48	Restart at the 48 h mark with 50% decrease of the solar constant
1.5×SW48	Restart at the 48 h mark with 50% increase of the solar constant
2×SW48	Restart at the 48 h mark with the doubling of the solar constant
NoSW	Restart at the 96 h mark with no solar radiation
0.5×SW	Restart at the 96 h mark with 50% decrease of the solar constant
1.5×SW	Restart at the 96 h mark with 50% increase of the solar constant
2×SW	Restart at the 96 h mark with the doubling of the solar constant

the “0.5×SW”, “1.5×SW”, and “2×SW” experiments to increase confidence in the simulated results and to reduce possible complications with inertia-buoyancy waves. With amplified heating rates due to a doubled solar constant, an enhanced inertial buoyancy wave response to that heating in the upper-troposphere is expected; however, this interesting feature does not impact the findings of this study. The same response of the SEF to the shortwave radiation is found when the diurnal cycle is removed and solar insolation was fixed (not shown). A second set of sensitivity tests are conducted by modifying the solar constant near sunset and sunrise instead of solar noon. Experiments with the solar constant changed at sunrise are referred to as the 90-h restarts and the experiments with changes to the solar radiation after sunset are referred to as the 102-h restarts. As will be shown later, these experiments result in a modification to the timing of the SEF proportional to the amount of time that the shortwave radiation has to modify the system. Despite slight differences in these sensitivity tests, the physical mechanisms remain the same and we posit that the conclusions of the study are not sensitive to the diurnal cycle or subdaily changes in the timing of the simulation restart time.

In the modeling framework used in this study, the sensitivity of the ERC to the cloud microphysics or radiation scheme cannot be directly determined because changes to those schemes from a restart file is not possible in WRF. The only feasible comparison is to run additional full physics simulations with the same initial conditions but different parameterizations. A comparison between the all-sky shortwave heating rates in

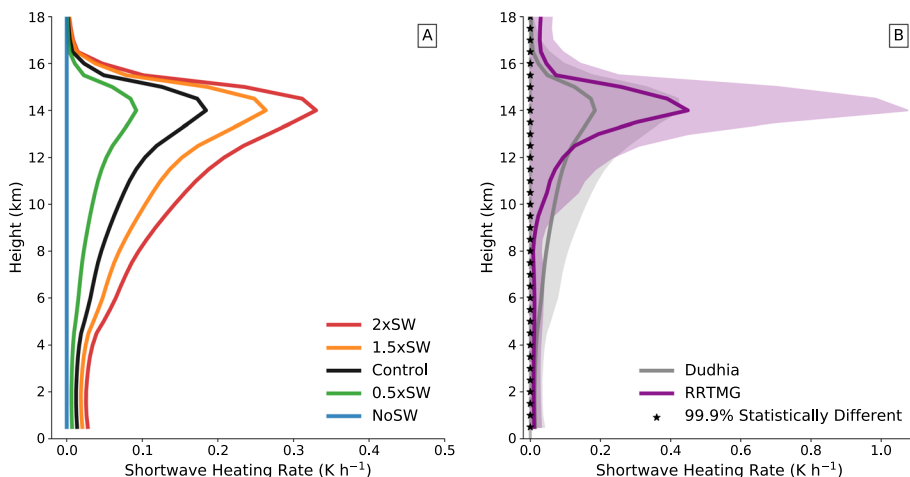


Figure 1. (a) The mean shortwave radiative heating profiles for radii greater than 150 km in the inner domain over the first 24 h following the 96-h restart experiments. A comparison between the Control experiment using the Dudhia scheme and a sensitivity test using the RRTMG scheme with the same initial conditions, temporal, and spatial time scales is shown in (b). The black stars indicate where the schemes are statistically different at the 99.9% confidence level using a two-sided T-test. The colored shading indicates the standard deviation of the shortwave schemes. Note that the shading of the standard deviation has been eliminated below zero since there are no shortwave cooling values.

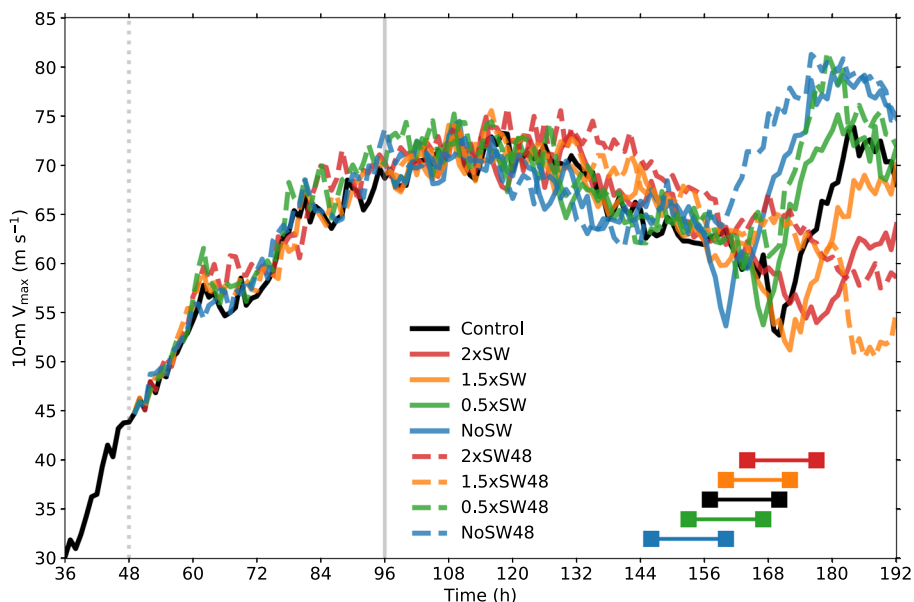


Figure 2. The temporal evolution of the 10-m maximum winds for each experiment. The dashed lines are the experiments with radiation modified 48 h into the simulation and the solid lines are the experiments with modified radiation after 96 h. The vertical gray lines indicate the time of radiative modification. The time frame between the development of a secondary wind maximum at 3 km altitude and the reintensification of the 10-m winds associated with the ERC are denoted for the 96 h experiments using their respective colors.

the experiments using the Dudhia scheme with another simulation using the RRTM for General Circulation Models (RRTMG; Iacono et al., 2008) scheme is shown in Figure 1b. The RRTMG scheme for shortwave radiation is a more advanced scheme that accounts for surface reflection and cloud overlapping which is not incorporated into the Dudhia scheme. Although the simulation with the RRTMG scheme does not have an ERC, we compare periods in the model where the simulated TCs are of similar size and intensity. Overall, the Dudhia scheme underestimates the peak heating rates and allows more shortwave radiation to be transmitted through the clouds compared to the RRTMG scheme. By amplifying the shortwave radiation in our 2xSW experiment, the peak in-cloud heating rates are actually brought closer to RRTMG values but with an increased bias in the amount of radiation transmitted through the upper-level clouds and absorbed in the mid-troposphere. Considering the large amounts of snow which are optically thicker than ice, a more peaked heating rate shown in the RRTMG simulation may be to first order more realistic. Tang et al. (2017) also employed the Dudhia scheme, but based on the differences between the Dudhia and RRTMG scheme, the upper-level response may be under-estimated and the low-level response may be over-estimated. In the current study we focus on the physical mechanisms induced by shortwave radiation on ERCs, with the acknowledgment that these mechanisms may be partially dependent on the specific parameterizations used. The sensitivity of convective and stratiform clouds during an ERC to the full parameter space of cloud microphysics schemes, radiation schemes, and boundary layer schemes is beyond the scope of this study but remains an important area for future work.

3. Impact of Shortwave Radiation on Wind Expansion and ERC

First we will explore the impacts shortwave radiation had on the intensity evolution during the ERCs of each experiment. Figure 2 shows the evolution of the 10-m maximum winds for each experiment listed in Table 1 with the black line indicating the Control. Here we define the ERC as beginning with the SEF at an altitude of 3 km and completing with the start of reintensification of the 10-m winds, which is denoted for each experiment in Figure 2 to orient the reader. To first order, there is little change to the TC intensity evolution in the 48 h restarts over the initial 48 h. The result suggests that the rapid intensification processes ongoing in the eyewall of the simulation are not affected by different shortwave heating magnitudes despite changes to the outer core thermodynamics at this time. Between the experiments, a consistent relationship

between shortwave heating and TC intensity does not manifest until the TCs begin to weaken slightly at the 120 h mark. Interestingly, the simulations which had more shortwave heating tend to be stronger than simulations without any shortwave heating. There are two possible explanations for this difference. The first explanation is that the shortwave heating in the canopy strengthened the upper-level secondary circulation that through mass conservation enhances the low-level inflow convergence of angular momentum. Although a stronger secondary circulation at upper-levels is evident in our simulations, consistent with recent literature and will be shown in Section 4, these anomalies remain primarily at the upper-levels and do not manifest themselves in stronger low-level radial winds (Navarro et al., 2017; Ruppert & O'Neill, 2019). Another explanation is that the larger amounts of shortwave radiative heating within the eye of the TCs can enhance the warm core. A stronger warm core is generally considered an indicator of a stronger TC with lower central pressure through hydrostatic balance (Ohno et al., 2016).

The completion of the ERC is related to the reintensification of the 10-m maximum winds but the reintensification rate can be dependent on the contraction of the secondary eyewall to smaller radii. The first TCs to reintensify are the NoSW48 and NoSW experiments followed by the 0.5×SW48 and 0.5×SW. These simulations had less shortwave radiation relative to the Control and the ERC completed earlier. The reintensification also occurs earlier in the 48-h experiments relative to the 96-h experiments indicating that the more time that the radiation has to modify the environment, the larger the effect on both the environment and the timing of the reintensification due to nonlinear feedbacks. In the experiments with more shortwave heating relative to the Control, the 1.5×SW and 2×SW experiments have a delayed reintensification suggesting that stronger shortwave heating rates over the diurnal cycle have a delaying effect on the ERC. A reintensification with the ERC does not occur in the 1.5×SW48 and 2×SW48 experiments within the simulation time frame but it is reasonable to assume that reintensification of some magnitude will occur if the simulations are extended. These simulations suggest that both the shortwave heating magnitude over the diurnal cycle and the duration over which this heating occurs has an important effect in modifying the timing of the onset and conclusion of ERCs. Because the reintensification associated with ERC and the contraction of the RMW did not complete before the end of all of the 48 h restart simulations, most of the discussion henceforth will be on the 96-h restarts.

Figure 2 also suggests that there is a relationship between shortwave radiation magnitude and the maximum intensity following the completion of the ERC. The maximum intensity of the NoSW experiment following the ERC is approximately 5 m s^{-1} stronger than the 0.5×SW experiment which is slightly stronger than the Control. The maximum intensity following the ERC of the 1.5×SW and 2×SW case are 5 m s^{-1} and 10 m s^{-1} weaker compared to the Control respectively. Although this relationship between the magnitude of shortwave heating and the maximum intensity after the ERC is suggested, it is difficult to assess the significance given the changes in the thermodynamic environment and the transition toward a new equilibrium state. The differences in intensity are due to a combination of factors including changes to the environment, the magnitude of convective diabatic heating within the new eyewall, and differences in the RMW. Figures 3a and 3b shows the evolution of the the RMW and select tangential wind contours for the 96-h restart experiments at an altitude of 1 km. The RMW for the 2×SW and 1.5×SW is shifted toward slightly larger radii relative to the 0.5×SW and NoSW experiments following the expansion of the RMW suggesting that the intensity differences after reintensification are, to a small degree due to changes in the RMW. What physical mechanisms govern the size of the RMW after the ERC is an open question that is outside the scope of the present study, but it will be shown later that the post-ERC RMW may be related to the radial distribution of convection and the intensity of the convection in the new eyewall. The 102 h Restarts in Figure 3c did not show consistent differences in the post-ERC RMW, but also had the least amount of time for differences in shortwave radiation to modify the thermodynamic environment. The change in post-ERC RMW may also relate to the changes in the overall vortex structure, boundary layer dynamics, and thermodynamic environment (Stern et al., 2015; Martinez et al., 2020).

The axisymmetric tangential winds shown in Figure 3 confirm that the tangential winds broaden prior to the eyewall replacement cycle which is consistent with previous observations (Sitkowski et al., 2011; Wu et al., 2012). Here we show the broadening occurs in the 96-h restart experiment in addition to the 90-h restart and 102-h restart sensitivity experiments. The 20, 30, and 45 m s^{-1} tangential wind contours all expand earlier in the experiments with less shortwave radiation relative to the Control (i.e., 0.5×SW and NoSW).

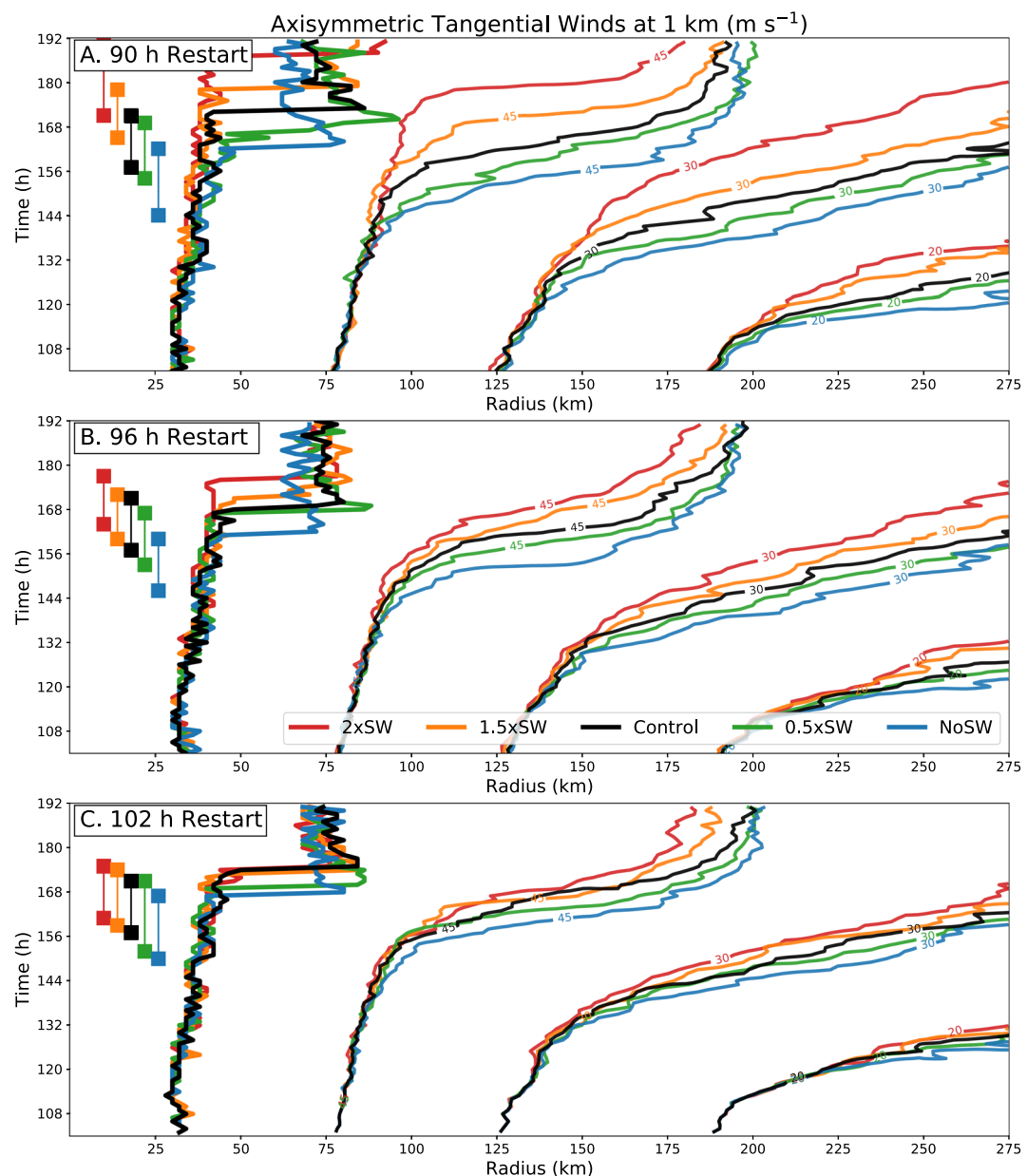


Figure 3. Hovmöller diagram of the 1-km axisymmetric tangential winds for the 96-h experiment (b) and the 90-h (a) and 102-h (c) restart sensitivity tests. Contours shown indicate the radii of 20, 30, and 45 m s⁻¹ tangential wind speeds. The RMW is denoted by the thicker radial contour line at the smallest radius. Tangential winds below 20 m s⁻¹ and exceeding 45 m s⁻¹ are removed for clarity. The time frame between the development of a secondary wind maximum at 3 km altitude and the reintensification of the 10-m winds associated with the ERC are denoted for each experiment using the colors corresponding to the magnitude of shortwave radiation.

which occurs in each of the three experiments shown. The expansion of the outer core tangential winds in the experiments occurs less than 12 h into the 96-h restart simulations and even sooner in the 90-h restarts. It should be noted that over the initial 48 h in all of the experiments there are no differences in the radius of the RMW, indicating that the effects of changes to the shortwave heating magnitude are first influencing the outer core radii beyond 150 km. This suggests that there is an alternative explanation on the differences in low-level tangential wind anomalies in the outer core on short time scales for SEF, besides the suppression of convection in the moat region by shortwave radiation as discussed in Tang et al. (2017). The overall

outward expansion of the tangential winds suggests there is strong rainband diabatic heating outside the eyewall region, while the magnitude of diabatic heating among the simulations is different.

The occurrence of the tangential wind expansion differences between each simulation is not sensitive to the timing of the radiative modification in Figure 3, although the magnitude of isotach differences between the experiments is sensitive. The 90-h restart experiments, where the changes to the shortwave radiation were made near sunrise, shows larger differences between the outward expansion of the radii of 20, 30, and 45 m s^{-1} winds compared to the 96-h restarts which in turn have larger differences compared to the 102-h restarts. In association with the larger differences in the expansion of tangential winds in the 90-h restarts, the timing of outward expansion of the RMW is also further modified. The 102-h experiments, in which the solar radiation is modified near sunset and the differences between the simulations over the following 12 h are only associated with stochastic convection, have only small differences between the timing of the SEF and the ERC. From the comparison of the SEF timing and the timing of intensification at the completion of the ERC in each experiment, the timing response of the SEF to the shortwave radiation is robust; however, there are no clear changes in the timing between the SEF and the reintensification following the completion of the ERC.

To understand what governs the initial expansion of the tangential winds, we analyze the evolution of the simulated 10-cm wavelength radar reflectivity and tangential winds in Figure 4. The reflectivity and tangential wind evolution are shown at an altitude of 3 km which is comparable to flight level observations (Sitkowski et al., 2011). The white contours show the radii where maximum shortwave heating is occurring, which is always collocated within the near-eyewall anvil cloud where the largest optical depths and shortwave flux convergence occur. Although maximum shortwave heating rates below 0.5 K h^{-1} are not shown, warming due to shortwave radiation does occur at all radii during daytime hours with varying magnitudes. Figure 4 shows that the SEF and ERC in the $2\times\text{SW}$ experiment occur later than those in the NoSW experiment in both the tangential winds and simulated axisymmetric mean reflectivity. Between hours 96 and 120, which is the first 24 h after the restarts, the axisymmetric mean simulated reflectivity beyond 150 km is stronger in the experiments with less shortwave radiation with larger reflectivities over several hours. As time progresses, the mean reflectivity in all the rainbands intensifies but the rainbands with more shortwave radiation have overall lower reflectivity values. Collocated with the stronger reflectivity beyond 150 km in the experiments with less shortwave heating is a faster expansion of the radii of 20 m s^{-1} tangential winds. Figure 4 suggests that the impacts of shortwave heating on the outer core rainband convection is a dominant factor contributing to differences in the timing of the tangential wind broadening consistent with the Tang and Zhang (2016).

Following the completion of the ERC when the TCs begin to reintensify, Figure 4 also shows structural differences that are related to the intensity differences in Figure 2. Consistent with the differences in the rainband strength prior to the SEF, the reflectivity within the new eyewall of the simulations with less shortwave radiation (NoSW and $0.5\times\text{SW}$) are higher compared to the Control. In association with the stronger convection, the NoSW and $0.5\times\text{SW}$ simulations have stronger tangential winds at 3-km compared to the $1.5\times\text{SW}$ and $2\times\text{SW}$ simulations. Outside of the new eyewall around hour 180, the NoSW and $0.5\times\text{SW}$ experiments have a larger area of reduced reflectivity values compared to the Control while the $2\times\text{SW}$ and $1.5\times\text{SW}$ experiments have a broader region of reflectivities $>32 \text{ dBZ}$. The intensity differences between each TC after the ERC is directly related to the strength of deep convection in the new eyewall which is anti-correlated with magnitude of the solar constant.

In this section, we have shown that shortwave radiation may impact the timing of SEFs and subsequent ERCS through the modification of outer core rainband convection. Together, these experiments confirm the sensitivity of SEFs to shortwave radiation discussed in Tang et al. (2017) in an idealized experiment, but further suggests that the stronger the magnitude of shortwave radiation and the longer amount of time that radiation has to impact the system, the larger the delay of the SEF. Because the timing of the SEF was delayed by shortwave radiation, the timing of the reintensification following the completion of the ERC was also delayed. The time from the generation of the SEF to the completion of the ERC was not significantly affected by changes to the shortwave radiation in the sensitivity experiments. The relationship between shortwave radiation and TC intensity following the completion of the ERC is complicated by small differences in the RMW, but is attributed to the stronger convection found in the new eyewall in the experiments

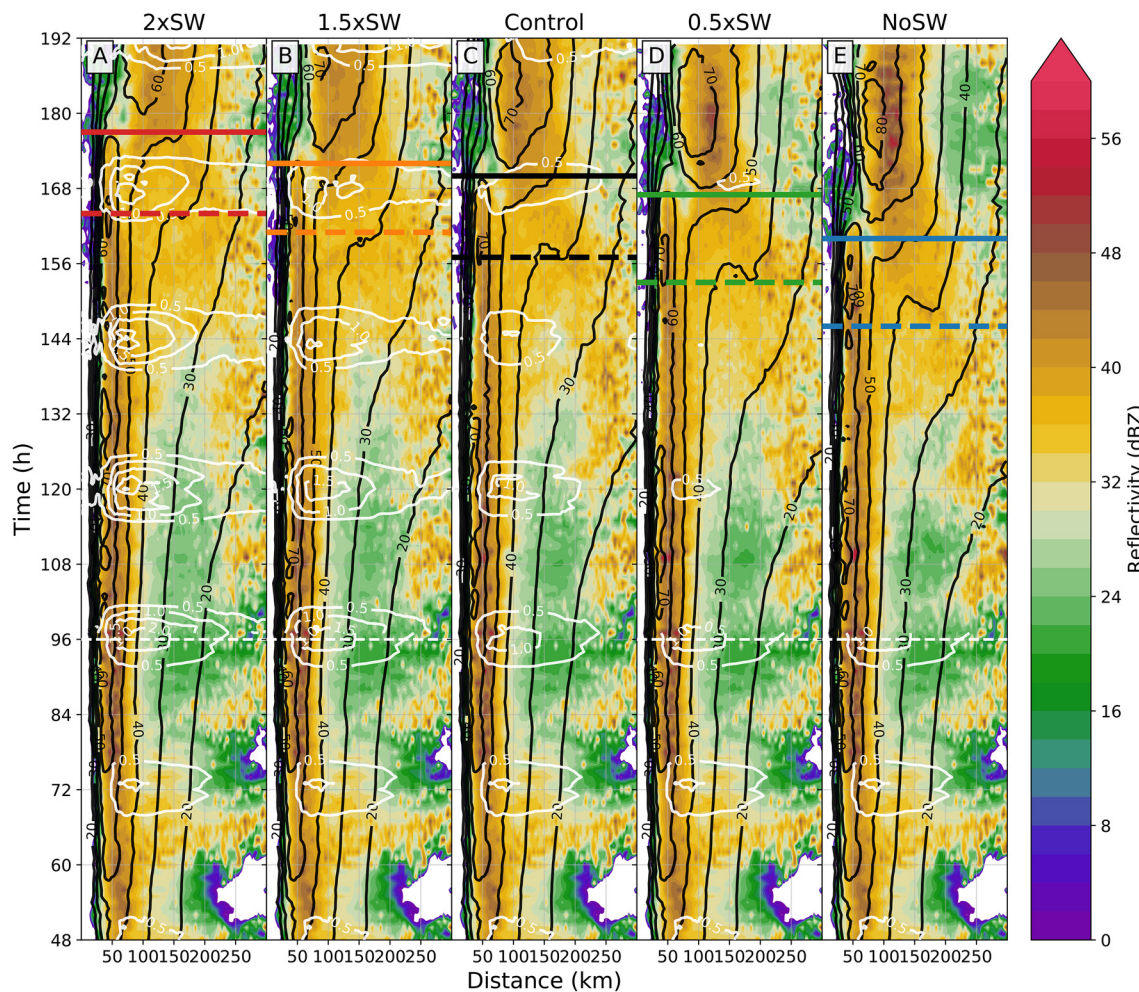


Figure 4. Hovmöller diagram of the 3-km axisymmetric reflectivity (shaded), 3-km tangential winds (black contour), and maximum shortwave heating (white contour) for the 2×SW (a), 1.5×SW (b), Control (c), 0.5×SW (d), and NoSW (e) experiments. Contour intervals are 2 dBZ, 10 m s^{-1} , and 0.5 K h^{-1} for reflectivity, tangential winds, and shortwave heating respectively. Tangential winds below 20 m s^{-1} and shortwave heating rates below 0.5 K h^{-1} are removed for clarity. The white dashed lines indicate when changes to the radiation were made in the experiments. The times corresponding to the development of the secondary wind maximum at an altitude of 3 km and the time of reintensification of the 10-m winds are denoted by the dashed and solid horizontal lines for each experiment respectively.

with less shortwave radiation. We will next explore potential mechanisms by which the shortwave radiation affects SEF timing by examining the structure and environment of the simulated TCs. Quantification of the effects of shortwave radiation on rainband convection will be shown in Section 5.

4. The Impact of Shortwave Radiation on TC Environment and Structure

We will now examine how shortwave radiation affects the structure of the TCs prior to the SEF and ERC. Figure 5 shows axisymmetric radius-height profiles of RH and radial winds in the early morning and late afternoon for the Control experiment and corresponding anomalies between experiments. The anomalies are plotted such that Figures 5c and 5d is the difference between one solar cycle and Figures 5e and 5f is the difference between two solar cycles in regards to the magnitude of shortwave heating. In the early morning the RH anomalies are generally less than 3% with some larger RH anomalies corresponding to slight differences in the slope of the eyewall. The larger RH differences occur in the late afternoon and are present in both the anomalies of 1.5×SW from 0.5×SW and 2×SW from NoSW. Here, the important differences are where the anomalies are consistent with sign between Figures 5d and 5f. There appears to be an increase in RH in the eyewall region with stronger shortwave radiation particularly at mid-levels which is during

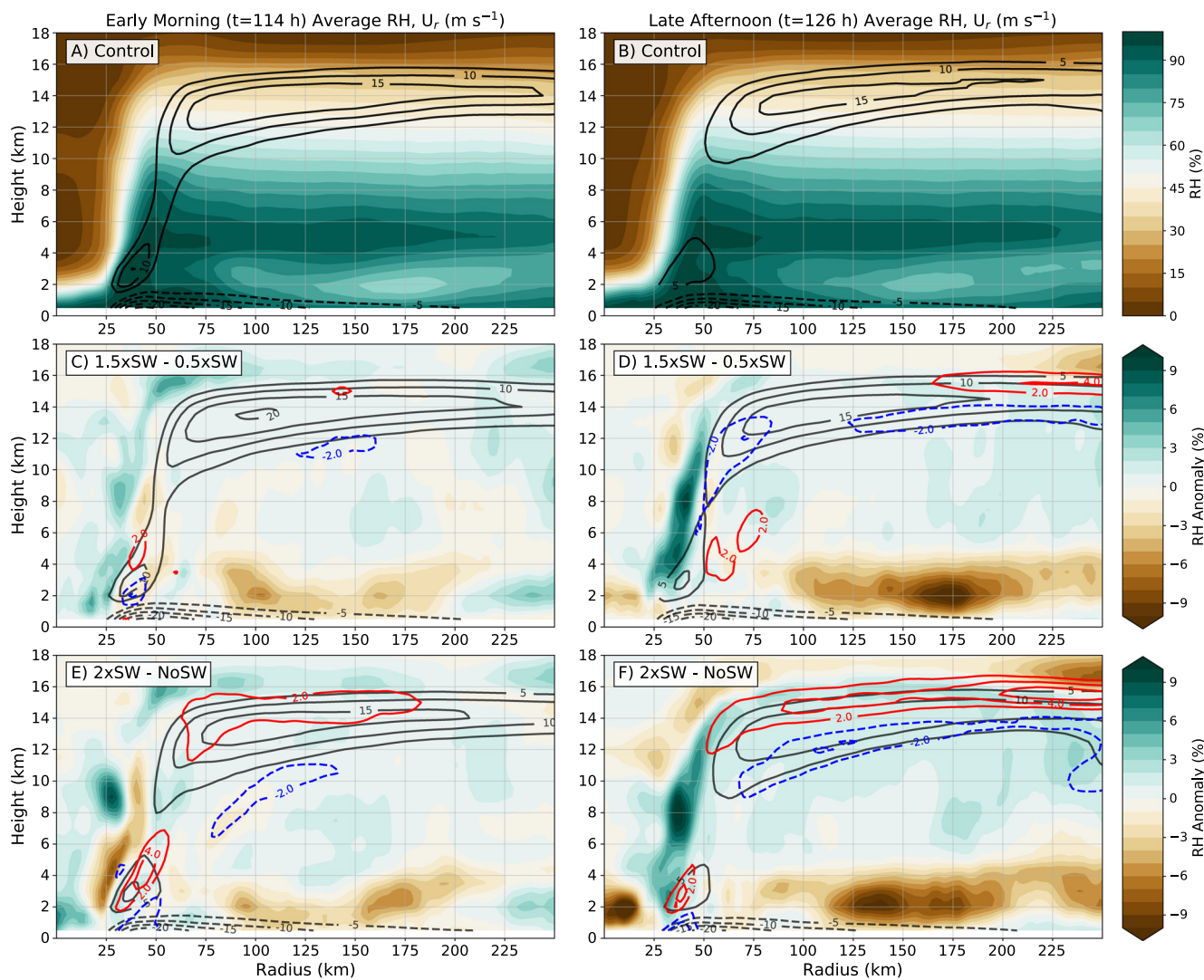


Figure 5. Axisymmetrized cross sections of the RH (shaded) and radial winds (contoured) for the Control experiment during the early morning (a) and late afternoon (b). RH is shaded at 5% intervals while the radial wind is contoured every 5 m s⁻¹ with the zero line removed for clarity. The time periods are a three hour average centered at the specified time to help smooth differences due to convection. The RH anomalies of the 1.5×SW experiment from the 0.5×SW experiment are shown for the early morning (c) and late afternoon (d) with the anomalies of the 2×SW experiment from the NoSW experiment shown for the same times in (e) and (f). The RH anomalies are contoured every 1% and the black radial wind contours are the reference state of the experiment being subtracted (i.e., 0.5×SW in [c and d] and NoSW in [e and f]) for the given time period. The radial wind anomalies are contoured every 2 m s⁻¹ with the zero line removed and red and blue colors representing positive and negative anomalies respectively.

an overall period of weakening as indicated by Figure 2. Figure 6 shows the same time period as Figure 5 but highlights the temperature and tangential wind differences between the models. The mean tangential winds in the eyewall through a deep portion of the troposphere decreased by 2–4 m s⁻¹, further supporting that the eyewall RH differences are due to a weakening primary eyewall in the NoSW and 0.5×SW experiments. There is a noticeable reduction in RH below 5 km in the region between 100 to 250 km radius (Figures 5d and 5f). The region below 5 km between 100–250 km radii also shows increased temperatures in Figures 6d and 6f indicating that the net warming and drying can be largely attributed to enhanced shortwave radiation. The RH differences maximize around 2 km and are reduced closer to the surface and actually reverse above 5 km. The RH differences at low-levels in the 100–175 km range are also evident in the early morning time periods with a weaker magnitude indicating that this effect may not be solely due to shortwave heating, although shortwave heating seems to exacerbate the anomalies.

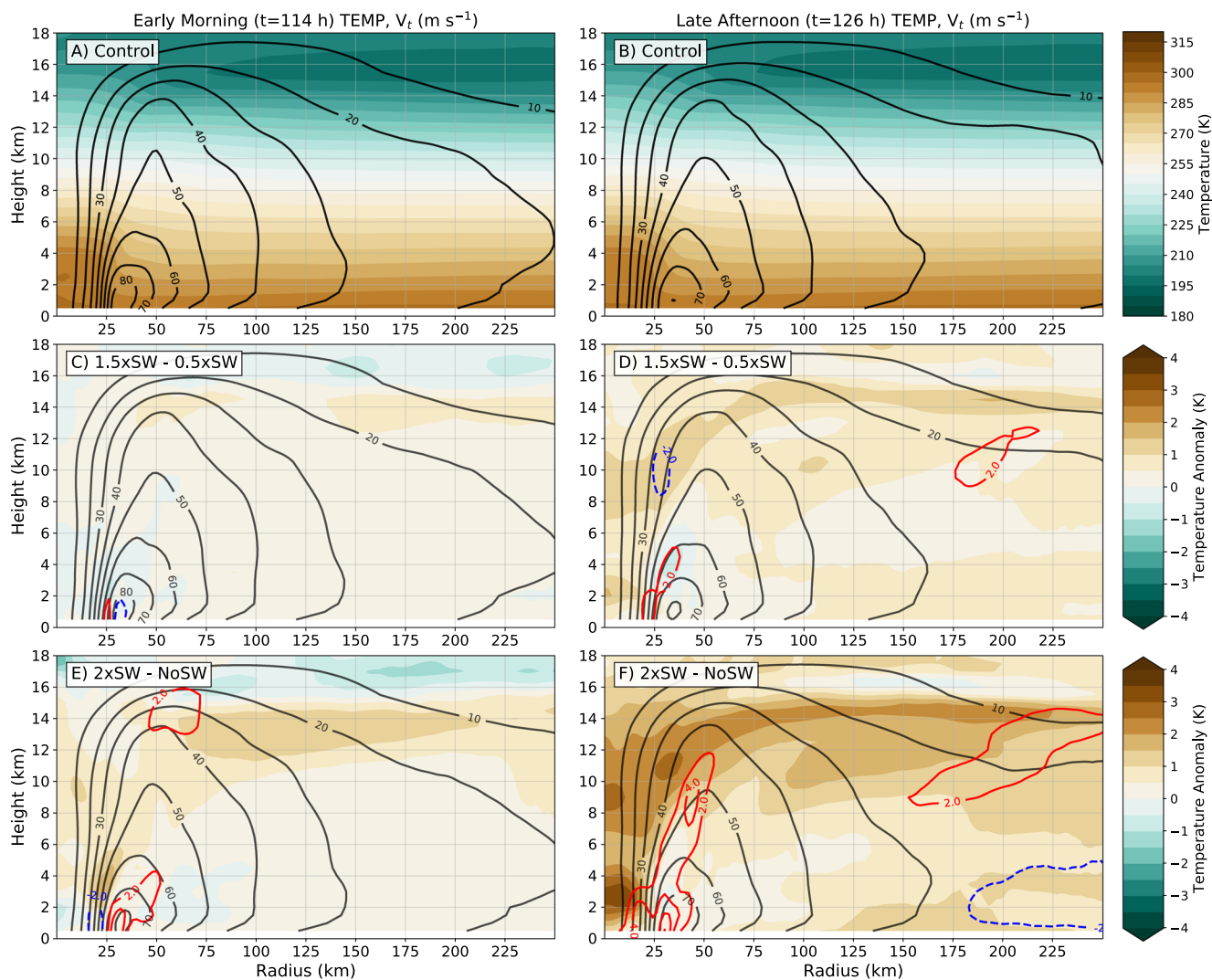


Figure 6. Same as Figure 5 but for temperature shaded every 5 K and tangential wind contoured every 10 m s⁻¹ in the Control experiment. Temperature anomalies are contoured at 0.5 K intervals with tangential wind anomalies every 2 m s⁻¹ with the zero line removed.

In Figure 5 there are differences in the radial winds, particularly in the outflow layer due to differences in shortwave heating in the late afternoon. The role of shortwave heating in the cirrus canopy and the influence on the TC outflow in relation to diurnal pulses (Dunion et al., 2014), remains an active area of research. Increases in the shortwave radiative heating in the cirrus canopy do induce changes in the outflow which are consistent with the Eliassen model (Eliassen, 1952) with an anomalous outflow above the heating and anomalous inflow below the heating, but there is only a small effect on the peak outflow values. In this framework, it appears that the stronger shortwave heating causes an increase in the overall height of the outflow layer which is consistent with the thermally direct circulation response to shortwave heating shown in Ruppert and O'Neill. (2019). Overall the changes to the radial winds due to changes in shortwave radiation were larger than any changes in the primary circulation shown in Figure 6. In the late afternoon there are stronger temperature anomalies as expected, which tend to maximize at upper levels due to solar absorption by optically thick clouds. Large temperature differences are also found in the eye of the TCs which at low levels can be attributed to shortwave absorption in the near-infrared by water vapor. The temperature anomaly at the upper-level warm core in Figures 6d and 6f are related to differences in the weakening trend of TCs prior to the development of the secondary eyewall. The strong anomalies in the eye are associated with an overall stronger storm in the 2xSW case relative to the NoSW. As noted in the previous section, the stronger warm core and outflow anomalies would both support the slightly stronger intensities in the

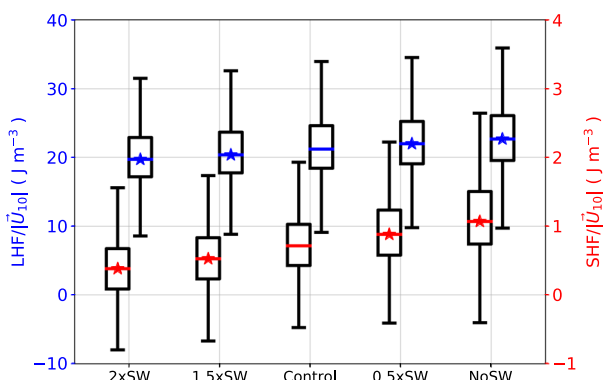


Figure 7. Box-and-whisker plot of latent heat fluxes and sensible heat fluxes normalized by the magnitude of the 10-m winds for each of the 96-h restart experiments over the first 36 h of the simulations beyond 150 km radii. The red and blue lines indicate the median of the normalized sensible and latent heat fluxes using the right and left ordinate respectively. The lower and upper quartile ranges are shown by the box while the whiskers extend 1.5 times the width of the box. Outliers beyond 1.5 times the width of the box are removed for clarity. The stars indicate that the mean of the sample is statistically significant from the Control at the 99.9% confidence level using a two-sided T-test.

TC with a cirrus canopy overhead in the 96-h restart, so clear-sky diurnal changes to the thermodynamic environment do not apply over a large region. The clear-sky thermodynamic modification mechanism may still be important at longer simulation times and at larger radii, but not over the first 48 h. Another mechanism that has been proposed to explain the diurnal cycle of precipitation in the tropics is by Gray and Jacobson (1977) in which differential cooling between cloudy and clear skies results in a pressure driven inflow that enhances the cloud scale circulation. In our experiments changes to the TC inflow on a diurnal basis are not found, although some recent observational evidence using dropsonde measurements does suggest a diurnally varying inflow (Zhang et al., 2020). In the current study, the mechanisms described by Melhauser and Zhang (2014) and Gray and Jacobson (1977) appear to be of secondary importance. It should also be mentioned that there were no systematic differences in the longwave warming across experiments such that changes in the outflow layer could not be driven by the mechanism explained in Bu et al. (2014).

The temperature differences due to the changes in shortwave heating rates are important at the upper-levels for changing the static stability, while the temperature differences near the surface can modify the air-sea disequilibrium. Both the modifications to the surface enthalpy fluxes and the changes to the upper-level static stability are important in controlling the strength of convection in the rainbands which has been shown to be important for the generation of secondary wind maxima and SEF (Zhu & Zhu, 2014). Figure 7 shows a box-and-whisker plot of the wind normalized sensible and latent heat fluxes for each experiment for radii greater than 150 km. The box-and-whisker plots all have statistically significant means that are different from the Control at the 99.9% confidence level. The simulations with more shortwave heating yield weaker wind normalized sensible and latent heat fluxes which can be attributed to a weaker equivalent potential temperature disequilibrium across the air-sea interface. The relationship between wind normalized enthalpy fluxes and shortwave heating is due to the near surface temperature being warmed at higher rates in the 2xSW and 1.5xSW experiments relative to the Control and is amplified after every diurnal cycle due to the radiation energy imbalance. It is important to note that one of the idealizations of this work is that the sea surface temperature is fixed, therefore excessive shortwave heating reaching the ocean surface and not being reflected cannot increase SST. Regardless, changes in SST are not likely to change the results of this study given that excess shortwave radiation reaching the sea surface would be mixed downwards into the ocean by the strong winds and slightly offset upwelling of colder subsurface water (Thompson et al., 2018). If the surface enthalpy fluxes are not normalized by wind speeds, the differences in the domain integrated amount of surface fluxes would be considerably larger for the NoSW and 0.5xSW experiments relative to

2xSW experiment; however, since there are no systematic differences in the inflow, the shortwave heating in the eye seems to be the cause of the intensity differences prior to the SEF.

Overall, Figures 5 and 6 are highlighted to show that there are few differences in the dynamics of the TC caused on short time scales by the stronger shortwave heating imparted on the storms. Similar to what has been shown by Navarro et al. (2017) and Ruppert and O'Neill (2019), the differences in circulation are primarily in the outflow layer due to shortwave heating anomalies, which do not induce strong tangential wind responses at low-levels that affect TC intensity. There are however, significant thermodynamic differences between the models due to the changes in shortwave heating magnitudes at both upper-levels and low-levels. The low-level reduction in RH in the simulations with larger shortwave heating is associated with weaker evaporation rates in the microphysics scheme which will be shown in the following section. The changes to low-level RH feeds back onto the timing of the SEF, but is not the mechanism controlling the differences in SEF timing.

Previous studies including Melhauser and Zhang (2014) have shown that shortwave radiation has a negative impact on the thermodynamic environment of TCs which inhibits tropical cyclogenesis. The changes to the thermodynamic environment play a role in the 48 h restarts; however, unlike Melhauser and Zhang (2014) we already have a well-established

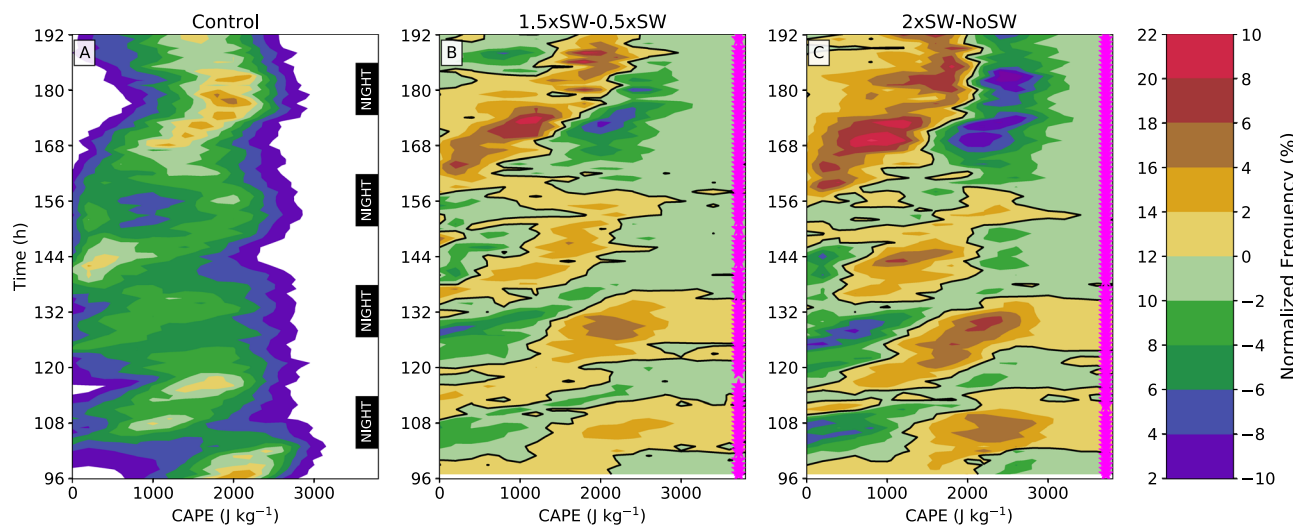


Figure 8. Temporal evolution of the distribution of CAPE binned over 100 J kg^{-1} intervals at radii greater than 150 km in the innermost domain. The distribution of CAPE is normalized by the sum of all values over each hour with values that make up less than 2% removed in the Control shown in (a). The anomalies of the $1.5\times\text{SW}$ from the $0.5\times\text{SW}$ experiment is shown in (b) and the $2\times\text{SW}$ anomalies from the NoSW experiment is shown in (c). The black line highlights the zero anomaly line. The left side of the colorbar is representative of the temporal evolution of CAPE in the Control experiment while the right side of the colorbar is representative for the anomalies. The black rectangles highlight the times without shortwave radiation. The pink stars on the right-hand side of (b and c) indicate the times where the means of the CAPE distributions shown are statistically different at the 99% confidence level using a two-sided T-test.

the control and reduced in the $1.5\times\text{SW}$ and $2\times\text{SW}$ experiments because of the differences in timing between the tangential wind expansion (not shown). Cheng and Wu (2018) found that a reduction in the surface fluxes in the region near and radially outside of the SEF similarly caused a delay in the timing of their idealized ERCs; however, the differences in fluxes between the experiments in this study are not as dramatic at the beginning of the experiments and affect a larger area. The nonlinear relationship between fluxes, convective generation and the increase in wind speeds is considered to be important for the changes in SEF timing as the TC wind field expands at different times, but because the differences are small and a response to early changes in deep convection, the fluxes are not directly responsible for the initial differences in tangential wind expansion.

Studies such as Xu and Wang (2010) and Cheng and Wu (2018) have suggested that surface sensible and latent heat fluxes are important for generating surface based CAPE which is then consumed by convection resulting in increased diabatic heating and subsequent changes to the tangential winds (Wang, 2009). Figure 8 shows the evolution of the distribution of surface based CAPE values for the Control and the anomalies for the experiments with the modified shortwave heating rates. We preferentially show the distribution of CAPE instead of the average values which can be misleading because CAPE is lowered once it is consumed by convection. It is essential to note that in our case, the surface enthalpy fluxes are not the only factor affecting the distribution of CAPE as any heating at the surface or cooling of the tropospheric temperature profile from radiation could increase CAPE. In the Control experiment, there is a large distribution of CAPE values between 1000 to 3000 J kg^{-1} which increases in the following six hours before shifting toward lower CAPE values as the instability is consumed by convection. The distribution of CAPE then increases again with continuous surface fluxes before once again being consumed leading to cyclic changes between convective development/invigoration and CAPE.

In Figures 8b and 8c, the anomalies of the $1.5\times\text{SW}$ from the $0.5\times\text{SW}$ experiment and $2\times\text{SW}$ from the NoSW experiment are shown. In both subplots there is a slight shift in the distribution of CAPE over the first 6 h with the $2\times\text{SW}$ and $1.5\times\text{SW}$ having distributions shifted toward lower values of CAPE. The differences over the first 6 h can be attributed to differences in shortwave heating at upper-levels as this corresponds to the time when shortwave heating is still ongoing with heating profiles similar to that shown in Figure 1a. In the following 8 h (102–110 h) there is a reversal in the distribution of CAPE with the NoSW and $0.5\times\text{SW}$ having much lower CAPE values compared to the $1.5\times\text{SW}$ and $2\times\text{SW}$ experiment because the CAPE is being consumed by convection in the simulations with reduced shortwave heating. The consumption of more CAPE

in the NoSW and $0.5\times$ SW occurs at night even though there are no consistent or significant differences in the longwave radiative cooling and warming. The experiments with larger shortwave heating rates have larger CAPE values at this time that is not being consumed as quickly due to increased convective inhibition. Consistent with the Control there is then a cycling of the anomalies which seems to show that CAPE is consumed in the NoSW and $0.5\times$ SW at a faster rate than the $2\times$ SW and $1.5\times$ SW experiments through the end of the simulation. The distribution of CAPE values in the $2\times$ SW and $1.5\times$ SW is continually shifting toward lower values through the simulations which is expected because the overall temperature profile is warming due to an imbalance between shortwave heating and longwave cooling, which then directly reduces CAPE and also reduces the surface enthalpy fluxes.

Here we have shown that the dynamics of the primary and secondary circulation of the inner core of the TCs in each experiment vary little in the short term due to the changes in shortwave radiative forcing, but there are important changes to the thermodynamic environment. Shortwave heating stabilized the mid-upper levels having a negative impact on the distribution of CAPE. Subsequent modifications to the surface sensible and latent heat fluxes due to changing thermodynamics at the air-sea interface grow with time over each diurnal cycle and are further amplified by timing differences in the expansion of the tangential winds. In addition, there are RH anomalies at low levels in the outer core which have yet to be thoroughly explained because the magnitudes exceed what is expected by increasing temperature alone. The RH differences are likely due to interactions between shortwave radiation and the microphysics scheme, which will be highlighted in the next section. The following section will explore the relationship between shortwave radiation and the strength and distribution of convective and stratiform clouds in the outer core region prior to the ERCs.

5. Assessing the Changes to Convective and Stratiform Cloud Distributions

To determine how shortwave radiation directly or indirectly affected convective and stratiform clouds in the rainbands, a partitioning algorithm is employed. The convective-stratiform partition utilizes horizontal reflectivity gradients at an altitude of 2 km with thresholds based on Yuter and Houze (1997) and Steiner et al. (1995). The simulated reflectivity using the Thompson aerosol-aware microphysics scheme has been shown to create realistic reflectivity profiles by Brown et al. (2014) and the partitioning is not sensitive to modest changes in the tunable parameters. This classification technique was compared with an updated version of the algorithm from Powell et al. (2016), which generates qualitatively similar results. We present the older algorithm because it employs fewer raintype classifications that are more stable for shorter timescales to allow for consistent time series.

The convective-stratiform partition was implemented only on the high resolution inner domain of the experiments and subcategorized based on radii from the TC centers. It is important to note a few limitations of the partitioning algorithm. Since the scheme is implemented at the 2-km level, the most homogeneous part of our profiles will be at 2-km and will become more heterogeneous at altitudes above and below this layer. Because the algorithm is based on one layer, we must assume that the classification is valid for all the grid cells in that column and as such highly tilted convection may not be well resolved. However, convection in the model does not exhibit significant tilt and the partition assumes a convective radius such that multiple grid cells around a resolved convective core will be classified as convective. The same scheme is used on all of the experiments and normalized by the number of events in each experiment.

The temporal evolution of the frequency of both convective and stratiform classified echoes relative to the Control for the 96-h restart experiments is shown in Figure 9. The frequency of the echoes are integrated over the radii greater than 150 km in the inner domain and are smoothed using 10 iterations of a 1-2-1 filter with weights of 0.25, 0.5, and 0.25 respectively to improve figure readability. Over the first 6 h where shortwave heating differences are ongoing in the model, there is an immediate change in the frequency of convection. The $0.5\times$ SW and NoSW experiment both have a net increase in the number of convectively classified points while the $1.5\times$ SW and $2\times$ SW have a net reduction in the amount of convective classified points. Once the sun goes down and all the simulations have the same longwave cooling, the number of convective grid points in the region of interest become similar. The sun rises in the simulations around hour 114 and the convective area relative to the Control again decreases in the experiments with the stronger shortwave

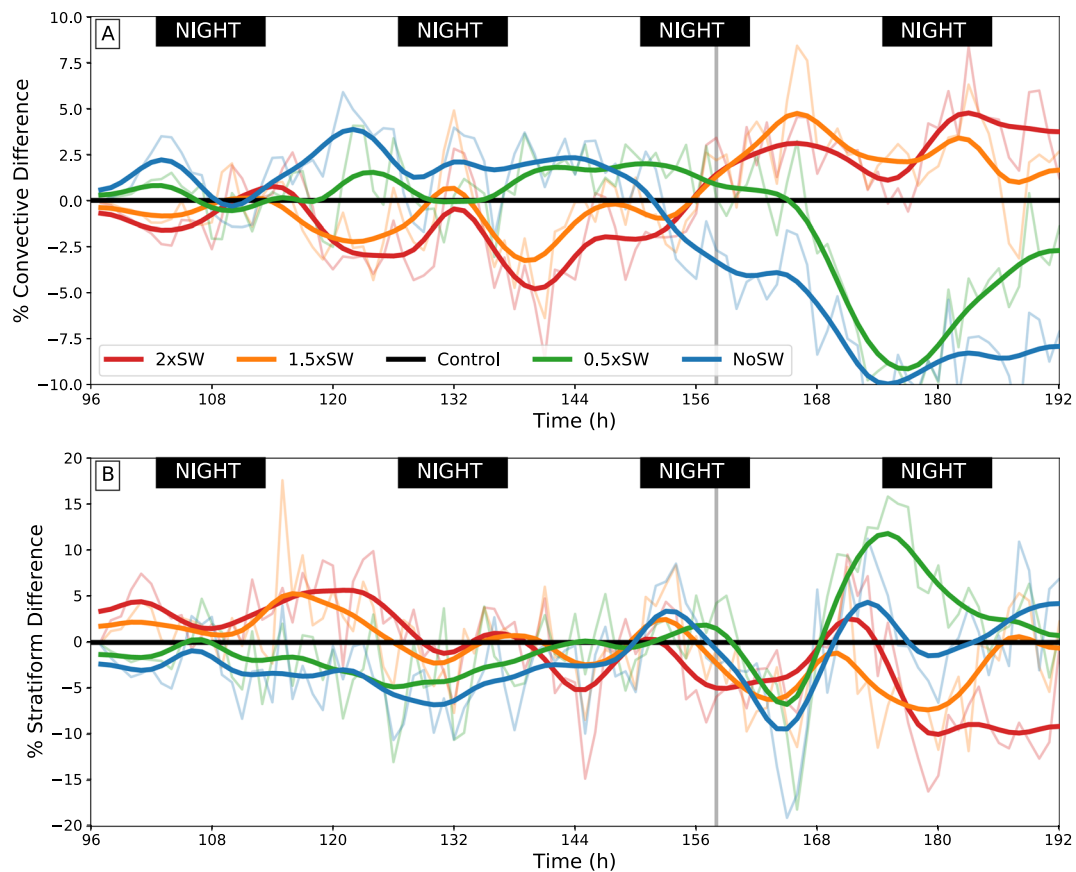


Figure 9. Temporal evolution of the areal frequency anomaly of convectively (a) identified radar echoes and stratiform (b) identified echoes from radii greater than 150 km in the 96-h restart experiments. The bold lines are filtered with 10 iterations of a 1-2-1 filter for clarity with the unfiltered data shown in the thinner and more transparent lines. The gray vertical lines indicate a rough estimate of the timing of the SEF in the NoSW experiment. The black rectangles highlight the times where shortwave radiation is not present.

radiation. At times beyond hour 158 indicated by the vertical line, the secondary eyewall has formed in the NoSW and $0.5\times$ SW simulations resulting in a decrease in the amount of convection at radii beyond 150 km, which makes comparing the TCs in this framework difficult. The overall change in convective frequency between the experiments prior to the ERC suggests a negative relationship between the magnitude of shortwave radiation and convective cloud amount due to changes in the mid-upper level static stability that was also suggested by the distribution changes of CAPE.

In Figure 9b, the response of stratiform clouds to shortwave radiation is opposite to that of convective clouds. The simulations with more shortwave radiation had a larger fraction of stratiform clouds during the day compared to the $0.5\times$ SW and NoSW experiments. To first order the differences can be explained by the decay of convective clouds into stratiform clouds as the shortwave heating stabilizes the upper levels. The stratiform clouds also tended to persist longer in the $2\times$ SW and $1.5\times$ SW experiments which is likely due to direct solar heating in the clouds amplifying the stratiform heating profile and vertical velocities in the upper-levels. The change in stratiform precipitation area is considered to be of secondary importance compared to the changes in convective area on the SEF.

In addition to affecting the area of convective and stratiform precipitation, shortwave radiation also affected the cloud microphysics. Figure 10 shows the vertical profiles of water vapor, rain, and snow mixing ratio anomalies for convective and stratiform identified clouds. The $2\times$ SW and $1.5\times$ SW simulations have reduced snow and rain mixing ratios while the experiments with less shortwave radiation have increased snow and rain mixing ratios in both convective and stratiform clouds. For convective clouds, associated with this reduction of snow and rain is an increase in the overall amount of water vapor with increased shortwave

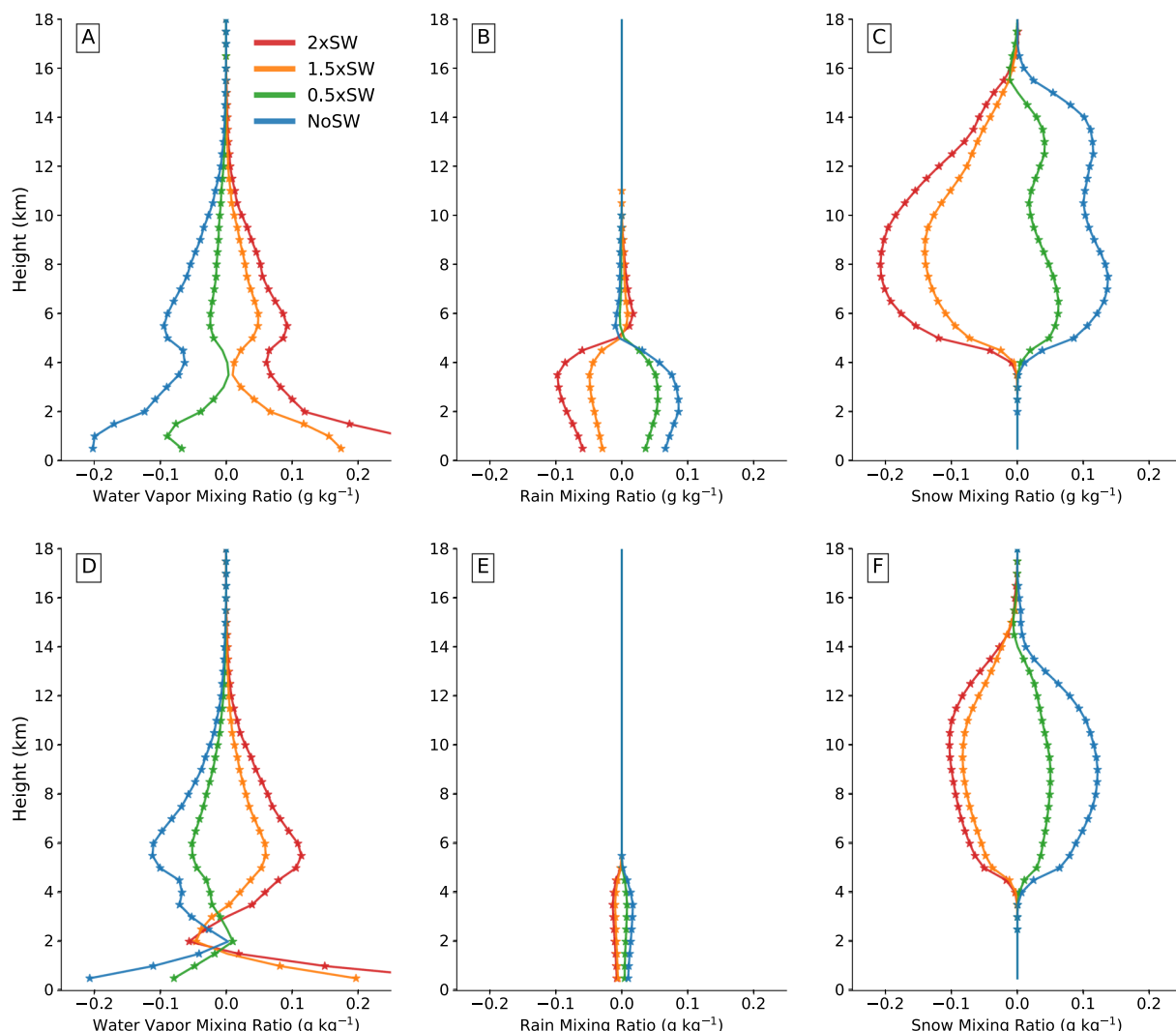


Figure 10. Vertical profiles of the mean water vapor (a), rain (b), and snow (c) mixing ratio anomalies from the Control experiment for convectively defined areas. The anomalies are computed for only convective areas at radii greater than 150 km in the innermost domain over the first 48 h of the 96-h restarts. The vertical profiles for water vapor, rain, and snow mixing ratio anomalies are shown for stratiform classified regions in (d), (e), and (f) respectively. The stars indicate where the mean mixing ratio is statistically different from the Control experiment at the 99% confidence level using a two sided T-test.

radiation. This suggests that solar absorption within the clouds is contributing to sublimation of snow and the evaporation of rain at mid-upper levels and explains the higher RH found at those levels in Figure 5. The overall convective heating profile from the microphysics is therefore reduced in the simulations with more shortwave radiation as shown by Figure 11b. Conversely, when the shortwave radiation is reduced in the 0.5×SW and NoSW simulations there is an increase in the amount of latent heating associated with the increase in snow and rain mixing ratios. This further suggests that with decreased solar radiation, the increase in diabatic heating from the microphysics in deep convective clouds is responsible for the faster generation of a secondary wind maximum.

The stratiform cloud profiles show a similar response to the shortwave radiation as the convective clouds but smaller in magnitude with reduced rain and snow mixing ratios associated with more shortwave radiation. The reduction in snow generation is associated with a reduction in the condensate heating shown in Figure 11a at upper levels. The reduction in rain mixing ratios below 5 km means that there is less rainfall that is able to evaporate contributing to a reduction in the evaporative cooling below the melting level. The reduction in snow above the melting level also contributes to less melting and weaker cooling rates. Overall there is a consistent relationship with stronger cooling due to evaporation and melting in the NoSW and

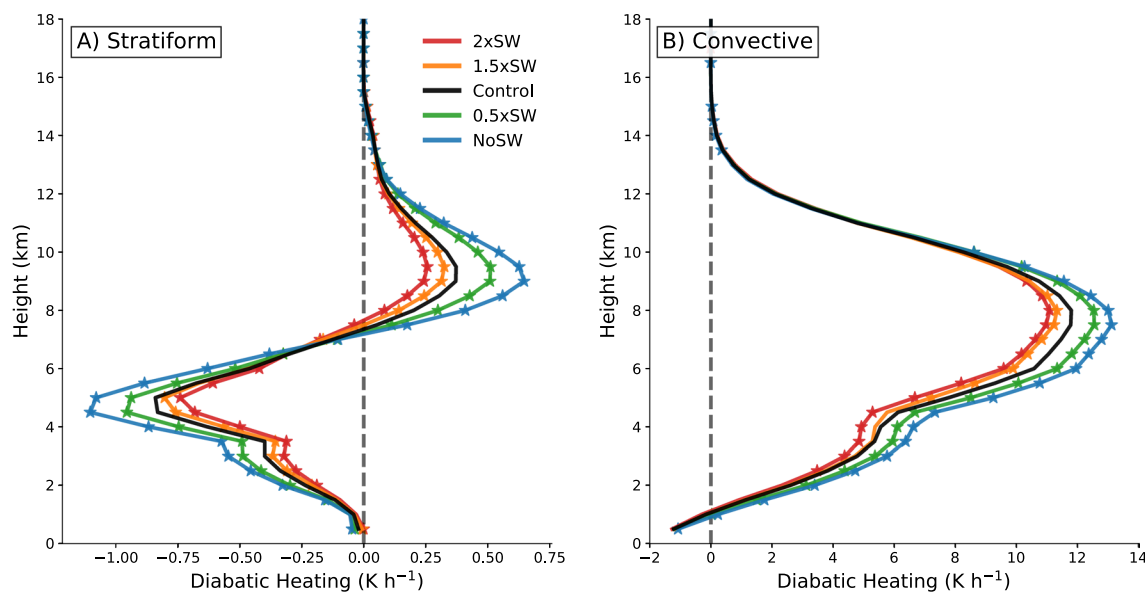


Figure 11. Vertical profiles of the diabatic heating rate from each of the experiments in areas classified as stratiform (a) and convective (b). The heating profiles are computed for only areas at radii greater than 150 km in the innermost domain over the first 48 h of the 96-h restarts. The stars indicate where the mean diabatic heating rate is statistically different from the mean of the Control experiment at the 99% confidence level using a two sided T-test.

0.5×SW experiment compared to the 1.5×SW and 2×SW experiment. Stronger cooling in the NoSW and 0.5×SW experiments means that stronger downdrafts can penetrate into the subcloud layer and enhance the surface sensible and latent heat fluxes. The opposite occurs in the 2×SW and 1.5×SW simulations where weaker downdrafts may not penetrate into the subcloud layer, contributing to the differences in fluxes shown in Figure 7. The differences in water vapor of stratiform clouds near 2 km is also evident in the low RH anomalies found in Figure 5, which can partially be explained by the transition between convective and stratiform precipitation. The weaker evaporation rates cause less water vapor in this region. It is unlikely that the water vapor anomalies at 2 km are an artifact of the convective-stratiform partition which is run at that level.

Rios-Berrios (2019) also found that the radiation-microphysics interactions, particularly in reference to rain evaporation, are a major source of uncertainty in numerical models and will be the focus of future work.

6. Conclusions

Recent work has shown that both shortwave and longwave radiation has important impacts on tropical cyclone structure, intensity, and track (Fovell et al., 2016). In this study we have used idealized WRF simulations to test the sensitivity of secondary eyewall formations and eyewall replacement cycles to diurnal shortwave radiation. This study has shown that shortwave radiation modifies the timing of secondary eye-wall formation and TC intensity following the completion of eyewall replacement cycles through its direct influence on convection in the rainbands. The strength of deep rainband convection as determined by the magnitude of diabatic heating was reduced by shortwave radiation leading to reduced convergence of angular momentum and slower expansion of tangential winds. Although the stabilization of the moat region by shortwave heating in Tang et al. (2017) may be important for SEFs prior to moat formation, it does not appear to explain the differences in timing of the SEFs within the idealized simulations presented here. The different results in our experiment compared to Tang et al. (2017) could be because our TCs were more intense with the moat region being maintained by dynamically induced subsidence. The differences between studies could also be attributed to differences in the thermodynamic and dynamic environments, as the real case of Hurricane Edouard had horizontally heterogeneous thermodynamic profiles and included the presence of moderate vertical wind shear (Tang et al. [2017], Figure 2). We hypothesize that both the differences in timing of SEF and differences in TC intensity change during the ERC are due to the effects of shortwave radiation on rainband convection. The primary effect is not due to the direct radiative heating addition to

diabatic heating in the rainbands, but instead through the indirect modification of the microphysical heating rates through changes to the stability and large-scale thermodynamic environment.

On short time scales of less than 48 h, shortwave radiation modified the timing of the ERC first through a modification of the stability at upper-levels of the preexisting convective and stratiform clouds. The stronger the shortwave heating, the stronger the stabilizing effect within both the convective and stratiform clouds which causes a reduction in the cloud scale latent heating profiles in the simulations with more shortwave heating compared to those without any. The upper-level shortwave heating results in a reduction of convective area and an increase in the area of stratiform precipitation. The reduction in convective diabatic heating in the $2\times\text{SW}$ and $1.5\times\text{SW}$ experiments results in the generation of a weaker secondary wind maximum, which takes longer to develop. Over time, the secondary wind maximum differences are amplified by surface sensible and latent heat fluxes and the generation of CAPE (Tang et al., 2017; Cheng & Wu, 2018). At longer time scales (beyond 48 h) where the radiation has more time to modify the large-scale thermodynamic environment, the differences in the timing of the SEF are also delayed due to nonlinear feedbacks and multiple radiative-convective interaction mechanisms. Sensitivity experiments varying the solar constants near sunrise compared to near sunset further verifies that the amplitude of the differences between the experiments and the Control are directly related to the amount of shortwave heating available to modify the system.

In the framework of this study, where our experiments are constrained by the initial condition at the time of the simulation restart, we have not directly assessed the sensitivity to stochastic changes in convection. Assessing the sensitivity to stochastic changes in convection is difficult because small perturbations would have a limited impact on the already established vortex and convective rainbands. Small perturbations to the system might therefore overestimate our confidence in small magnitude differences between the experiments. Given that there was little to no change in the intensity of the simulated tropical cyclones for almost 48 h despite large differences in shortwave radiation, larger perturbations to the model to create an ensemble would likely overwhelm the radiative signal which aggregates over multiple diurnal cycles. Although the results of this study are based on single model runs with sensitivity experiments, given the ensemble variability due to stochastic perturbations in boundary layer moisture at model initialization of the system shown in Trabing et al. (2019), the differences in the timing of the SEF and subsequent ERC are robust. Further research should be considered on the role that radiation plays in ensemble variability, particularly for the purpose of gauging statistical significance.

This work suggests that regardless of the TC intensity, the diurnal cycle of radiation plays a role in the convective and stratiform nature of the rainbands that can then affect the TC intensity through ERCs. Although this study is based on a set of experiments with a single set of cloud microphysics and radiation schemes, the results suggest that the interactions between radiation schemes and microphysics schemes employed by operational models could lead to differences in ERCs that are explicitly simulated. The changes to the convective-stratiform distribution and associated heating profiles could then lead to errors in forecast estimates of wind radii and to TC intensity. Subsequent work is needed to test the additional sensitivities of radiation and cloud microphysics to the boundary layer scheme and ocean coupling. A complete sensitivity analysis between radiation schemes and the important interactions with the microphysics schemes will be the focus of future work.

Data Availability Statement

The model namelist and restart files required to reproduce the simulations analyzed herein can be accessed at <http://doi.org/10.5281/zenodo.4011043>.

References

- Bell, M. M., & Montgomery, M. T. (2019). Mesoscale Processes during the Genesis of Hurricane Karl (2010). *Journal of the Atmospheric Sciences*, 76, 2235–2255. <https://doi.org/10.1175/JAS-D-18-0161.1>
- Brown, B. R., Bell, M. M., & Frambah, A. J. (2016). Validation of simulated hurricane drop size distributions using polarimetric radar. *Geophysical Research Letters*, 43, 910–917. <https://doi.org/10.1002/2015GL067278>
- Bu, Y. P., Fovell, R. G., & Corbosiero, K. L. (2014). Influence of Cloud-Radiative Forcing on Tropical Cyclone Structure. *Journal of the Atmospheric Sciences*, 71, 1644–1662. <https://doi.org/10.1175/JAS-D-13-00265.110.1175/jas-d-13-0265.1>

Acknowledgments

The authors would like to thank Dr. Anthony Didlake Jr. and Dr. Dandan Tao for their insightful comments. This work has also been improved by three anonymous reviewers. This work has been funded by the Office of Naval Research Awards N000141613033, N000141712230, and N000142012069, and National Science Foundation award AGS-1701225.

- Cheng, C.-J., & Wu, C.-C. (2018). The Role of WISHE in Secondary Eyewall Formation. *Journal of the Atmospheric Sciences*, 75, 3823–3841. <https://doi.org/10.1175/JAS-D-17-0236.1>
- Craig, G. C. (1996). Numerical experiments on radiation and tropical cyclones. *Quarterly Journal of the Royal Meteorological Society*, 122, 415–422. <https://doi.org/10.1002/qj.49712253006>
- DeMaria, M., Mainelli, M., Shay, L. K., Knaff, J. A., & Kaplan, J. (2005). Further Improvements to the Statistical Hurricane Intensity Prediction Scheme (SHIPPS). *Forecasting*, 20, 531–543. <https://doi.org/10.1175/WAF862.1>
- Didlake, A. C., & Kumjian, M. R. (2018). Examining Storm Asymmetries in Hurricane Irma (2017) Using Polarimetric Radar Observations. *Geophysical Research Letters*, 45, 13,513–13,522. <https://doi.org/10.1029/2018GL080739>
- Didlake, A. C., Reasor, P. D., Rogers, R. F., & Lee, W.-C. (2018). Dynamics of the Transition from spiral rainbands to a secondary eyewall in Hurricane Earl (2010). *Journal of the Atmospheric Sciences*, 75, 2909–2929. <https://doi.org/10.1175/JAS-D-17-0348.1>
- Dudhia, J. (1989). Numerical Study of convection observed during the Winter Monsoon Experiment using a mesoscale two dimensional model. *Journal of the Atmospheric Sciences*, 46, 3431–3456. [https://doi.org/10.1175/1520-0469\(1989\)046<3431:nsoc>2.0.co;2](https://doi.org/10.1175/1520-0469(1989)046<3431:nsoc>2.0.co;2)
- Dunion, J. P., Thorncroft, C. D., & Velden, C. S. (2014). The Tropical Cyclone Diurnal Cycle of Mature Hurricanes. *Monthly Weather Review*, 142, 3900–3919. <https://doi.org/10.1175/MWR-D-13-00191.1>
- Eliassen, A. (1952). Slow thermally or frictionally controlled meridional circulations in a circular vortex. *Astrophysica Norvegica*, 5, 19–60.
- Fovell, R. G., Bu, Y. P., Corbosiero, K. L., Tung, W.-w., Cao, Y., Kuo, H.-C., et al. (2016). Influence of Cloud Microphysics and Radiation on Tropical Cyclone Structure and Motion. *Meteorological Monographs*, 56, 1. 11.1–11.27. <https://doi.org/10.1175/AMSMONOGRAPHSD-15-0006.1>
- Gray, W. M., & Jacobson, R. W. (1977). Diurnal variation of deep cumulus convection. *Monthly Weather Review*, 105, 1171–1188. [https://doi.org/10.1175/1520-0493\(1977\)105<1171:dvodcc>2.0.co;2](https://doi.org/10.1175/1520-0493(1977)105<1171:dvodcc>2.0.co;2)
- Herndon, D., Wimmers, A., & Kossin, J. (2020). *Upgrades to the M-PERC and PERC models to improve short term tropical cyclone intensity forecasts*. 74th Interdepartmental hurricane Conference 2020. Lakeland, FL, Feb 25–26. Retrieved from https://www.nhc.noaa.gov/jht/19-22reports/JHT1922_IHC_2020_Herndon.pdf
- Hong, S.-Y., Noh, Y., & Dudhia, J. (2006). A new vertical diffusion package with an explicit treatment of entrainment processes. *Monthly Weather Review*, 134, 2318–2341. <https://doi.org/10.1175/MWR3199.1>
- Houze, R. A., Chen, S. S., Smull, B. F., Lee, W.-C., & Bell, M. M. (2007). Hurricane Intensity and Eyewall Replacement. *Science*, 315, 1235–1239. <https://doi.org/10.1126/science.1135650>
- Huang, Y.-H., Montgomery, M. T., & Wu, C.-C. (2012). Concentric Eyewall Formation in Typhoon Sinlaku (2008). Part II: Axisymmetric Dynamical Processes. *Journal of the Atmospheric Sciences*, 69, 662–674. <https://doi.org/10.1175/JAS-D-11-0114.1>
- Iacono, M. J., Delamere, J. S., Mlawer, E. J., Shephard, M. W., Clough, S. A., & Collins, W. D. (2008). Radiative Forcing by long-lived greenhouse gases: Calculations with the AER radiative transfer models. *Journal of Geophysical Research*, 113, D13103. <https://doi.org/10.1029/2008JD009944>
- Kossin, J. P., & DeMaria, M. (2016). Reducing Operational Hurricane Intensity Forecast Errors during Eyewall Replacement Cycles. *Forecasting*, 31, 601–608. <https://doi.org/10.1175/WAF-D-15-0123.1>
- Martinez, J., Nam, C. C., & Bell, M. M. (2020). On the contributions of incipient vortex circulation and environmental moisture to tropical cyclone expansion. *Journal of Geophysical Research - D: Atmospheres*, 125, e2020JD033324. <https://doi.org/10.1029/2020JD033324>
- Melhauser, C., & Zhang, F. (2014). Diurnal radiation cycle impact on the pregenesis environment of hurricane karl (2010). *Journal of the Atmospheric Sciences*, 71, 1241–1259. <https://doi.org/10.1175/JAS-D-13-0116.1>
- Mlawer, E. J., Taubman, S. J., Brown, P. D., Iacono, M. J., & Clough, S. A. (1997). Radiative transfer for inhomogeneous atmospheres: RRTM, a validated correlated-k model for the longwave. *Journal of Geophysical Research*, 102, 16663–16682. <https://doi.org/10.1029/97JD00237>
- Navarro, E. L., Hakim, G. J., & Willoughby, H. E. (2017). Balanced Response of an Axisymmetric Tropical Cyclone to Periodic Diurnal Heating. *Journal of the Atmospheric Sciences*, 74, 3325–3337. <https://doi.org/10.1175/JAS-D-16-0279.1>
- Nicholls, M. E. (2015). An investigation of how radiation may cause accelerated rates of tropical cyclogenesis and diurnal cycles of convective activity. *Atmospheric Chemistry and Physics*, 15, 9003–9029. <https://doi.org/10.5194/acp-15-9003-2015>
- Ohno, T., Satoh, M., & Yamada, Y. (2016). Warm cores, eyewall slopes, and intensities of tropical cyclones simulated by a 7-km-mesh global nonhydrostatic model. *Journal of the Atmospheric Sciences*, 73, 4289. <https://doi.org/10.1175/JAS-D-15-0318.1>
- Powell, S. W., Houze, R. A., & Brodzik, S. R. (2016). Rainfall-Type Categorization of Radar Echoes Using Polar Coordinate Reflectivity Data. *Journal of Atmospheric and Oceanic Technology*, 33, 523–538. <https://doi.org/10.1175/JTECH-D-15-0135.1>
- Rios-Berrios, R. (2020). Impacts of Radiation and Cold Pools on the Intensity and Vortex Tilt of Weak Tropical Cyclones Interacting with Vertical Wind Shear. *Journal of the Atmospheric Sciences*, 77, 669–689. <https://doi.org/10.1175/JAS-D-19-0159.1>
- Rotunno, R., & Emanuel, K. A. (1987). An air-sea interaction theory for tropical cyclones. Part II: Evolutionary study using a nonhydrostatic axisymmetric numerical model. *Journal of the Atmospheric Sciences*, 44, 542–561. [https://doi.org/10.1175/1520-0469\(1987\)044<0542:aaift>2.0.co;2](https://doi.org/10.1175/1520-0469(1987)044<0542:aaift>2.0.co;2)
- Ruppert, J. H., & O'Neill, M. E. (2019). Diurnal Cloud and Circulation Changes in Simulated Tropical Cyclones. *Geophysical Research Letters*, 46, 502–511. <https://doi.org/10.1029/2018GL081302>
- Sitkowski, M., Kossin, J. P., & Rozoff, C. M. (2011). Intensity and structure changes during hurricane eyewall replacement cycles. *Monthly Weather Review*, 139, 3829–3847. <https://doi.org/10.1175/MWR-D-11-00034.1>
- Skamarock, W. C., & Coauthors (2008). A description of the Advanced Research WRF version 3, NCAR Tech. Note NCAR/TN-475+STR, 113. <https://doi.org/10.5065/D68S4MVH>
- Steiner, M., Houze, R. A., & Yuter, S. E. (1995). Climatological characterization of three-dimensional storm structure from operational radar and rain gauge data. *Journal of Applied Meteorology and Climatology*, 34, 1978–2007. [https://doi.org/10.1175/1520-0450\(1995\)034<1978:ccotds>2.0.co;2](https://doi.org/10.1175/1520-0450(1995)034<1978:ccotds>2.0.co;2)
- Stern, D. P., Vigh, J. L., Nolan, D. S., & Zhang, F. (2015). Revisiting the Relationship between Eyewall Contraction and Intensification. *Journal of the Atmospheric Sciences*, 72, 1283–1306. <https://doi.org/10.1175/JAS-D-14-0261.1>
- Sundqvist, H. (1970). Numerical simulation of the development of tropical cyclones with a ten-level model. Part II. *Tellus*, 22, 504–510. <https://doi.org/10.1111/j.2153-3490.1970.tb00516.x>
- Tang, X., Fang, Z.-M. J., Sun, Y. Q., & Zhang, F. (2017). Impact of the Diurnal Radiation Cycle on Secondary Eyewall Formation. *Journal of the Atmospheric Sciences*, 74, 3079–3098. <https://doi.org/10.1175/JAS-D-17-0020.1>
- Tang, X., & Zhang, F. (2016). Impacts of the Diurnal Radiation Cycle on the Formation, Intensity, and Structure of Hurricane Edouard (2014). *Journal of the Atmospheric Sciences*, 73, 2871–2892. <https://doi.org/10.1175/JAS-D-15-0283.1>
- Thompson, E. J., Moum, J. N., Fairall, C. W., & Rutledge, S. A. (2019). Wind limits on rain layers and diurnal warm layers. *Journal of Geophysical Research: Oceans*, 124, 897–924. <https://doi.org/10.1029/2018JC014130>

- Thompson, G., & Eidhammer, T. (2014). A study of aerosol impacts on clouds and precipitation development in a large winter cyclone. *Journal of the Atmospheric Sciences*, 71, 3636–3658. <https://doi.org/10.1175/JAS-D-13-0305.1>
- Tiedtke, M. (1989). A comprehensive mass flux scheme for cumulus parameterization in large-scale models. *Monthly Weather Review*, 117, 1779–1800. [https://doi.org/10.1175/1520-0493\(1989\)117<1779:acmf>2.0.co;2](https://doi.org/10.1175/1520-0493(1989)117<1779:acmf>2.0.co;2)
- Trabing, B. C., Bell, M. M., & Brown, B. R. (2019). Impacts of Radiation and Upper-Tropospheric Temperatures on Tropical Cyclone Structure and Intensity. *Journal of the Atmospheric Sciences*, 76, 135–153. <https://doi.org/10.1175/JAS-D-18-0165.1>
- Wang, H., Wu, C.-C., & Wang, Y. (2016). Secondary Eyewall Formation in an Idealized Tropical Cyclone Simulation: Balanced and Unbalanced Dynamics. *Journal of the Atmospheric Sciences*, 73, 3911–3930. <https://doi.org/10.1175/JAS-D-15-0146.1>
- Wang, Y. (2009). How Do Outer Spiral Rainbands Affect Tropical Cyclone Structure and Intensity? *Journal of the Atmospheric Sciences*, 66, 1250–1273. <https://doi.org/10.1175/2008JAS2737.1>
- Wu, C.-C., Huang, Y.-H., & Lien, G.-Y. (2012). Concentric Eyewall Formation in Typhoon Sinlaku (2008). Part I: Assimilation of T-PARC Data Based on the Ensemble Kalman Filter (EnKF). *Monthly Weather Review*, 140(2), 506–527. <https://doi.org/10.1175/MWR-D-11-00057.1>
- Xu, J., & Wang, Y. (2010). Sensitivity of tropical cyclone inner-core size and intensity to the radial distribution of surface entropy flux. *Journal of the Atmospheric Sciences*, 67, 1831–1852. <https://doi.org/10.1175/2010JAS3387.1>
- Xu, K.-M., & Randall, D. A. (1995). Impact of interactive radiative transfer on the macroscopic behavior of cumulus ensembles. Part II: Mechanisms for cloud-radiation interactions. *Journal of the Atmospheric Sciences*, 52, 800–817. [https://doi.org/10.1175/1520-0469\(1995\)052<0800:iort>2.0.co;2](https://doi.org/10.1175/1520-0469(1995)052<0800:iort>2.0.co;2)
- Yuter, S. E., & Houze, R. A. (1997). Measurements of Raindrop Size Distributions over the Pacific Warm Pool and Implications for Z-R Relations. *Journal of Applied Meteorology and Climatology*, 36, 847–867. [https://doi.org/10.1175/1520-0450\(1997\)036<0847:mrsdo>2.0.co;2](https://doi.org/10.1175/1520-0450(1997)036<0847:mrsdo>2.0.co;2)
- Zhang, J. A., Dunion, J. P., & Nolan, D. S. (2020). In situ observations of the diurnal variation in the boundary layer of mature hurricanes. *Geophysical Research Letters*, 47, e2019GL086206. <https://doi.org/10.1029/2019GL086206>
- Zhu, Z., & Zhu, P. (2014). The role of outer rainband convection in governing the eyewall replacement cycle in numerical simulations of tropical cyclones. *Journal of Geophysical Research - D: Atmospheres*, 119, 8049–8072. <https://doi.org/10.1002/2014JD021899>